Available online at www.sciencedirect.com
ScienceDirect
Journal of Sound and Vibration 321 (2009) 492–509
JOURNAL OF SOUND AND VIBRATION
www.elsevier.com/locate/jsvi

Numerical investigation on active isolation of ground shock by soft porous layers

J.G. Wang*, W. Sun, S. Anand

Centre for Protective Technology, Department of Civil Engineering, National University of Singapore, Singapore 119260, Singapore

Received 20 August 2007; received in revised form 26 September 2008; accepted 27 September 2008
Handling Editor: L.G. Tham
Available online 12 November 2008

Abstract

The mitigation and reduction of blast-induced ground shock in near field is an interesting topic worth considering for the protection of buried structures. Soft porous materials are usually used to form an isolation layer around the buried structures. However, the interaction of soft porous layer and surrounding geomedia as well as buried structures is not well understood.

In this paper, the effects of soft porous layer barriers on the reduction of buried blast-induced ground shock are numerically studied. Based on the prototype dimensions of a centrifuge test, a numerical model is set up with two steel boxes symmetrically buried at two sides of the charge. One box is directly located in soil mass without protection (unprotected) and the other is located behind a soft porous layer barrier (protected). The soft porous layer barriers studied here include an open trench, an inundated water trench, three in-filled geofoam walls with different densities, and a concrete wall. The numerical responses of the two boxes are evaluated when subjected to the protection of different soft porous layer barriers. These numerical simulations show that both open trench and geofoam barriers can effectively reduce blast-induced stress waves. However, inundated water trench and concrete wall have almost no effect on the reduction of ground shock. Therefore, a geofoam barrier is more practicable in soil mass.

1. Introduction

The ground shock induced by the buried blast propagates in surrounding soil media. Its impact will affect adjacent buried structures even surface structures. This buried blast usually produces a crater and results in the interaction of surrounding soil media and detonation product gas. Furthermore, the propagation of blast-induced stress wave will induce the acceleration of soil particle and soil pressure in the surrounding soil media. If a buried structure is located near the blast source, the soil pressure and acceleration will result in severe damage or even the collapse of the structure, causing device failures or life loss. Therefore, the interaction between blast source and surrounding soil, the surrounding soil and nearby buried structures and the protection design of such buried structures are important issues in civil defense engineering.

*Corresponding author. Tel.: +65 6516 6591; fax: +65 6779 1635.
E-mail addresses: nuswjg@yahoo.com, cvewjg@nus.edu.sg (J.G. Wang).

0022-460X/$ - see front matter © 2008 Elsevier Ltd. All rights reserved.
doi:10.1016/j.jsv.2008.09.047

On the other hand, the near-field interaction of explosive-soil-barrier-buried structure is so complex that few publications can be found in public literatures. The near-field protection of buried structures through wave barriers is also an important topic in either the vibration control for high-speed train operation [1,2] or the damage control for blast events [3–5]. As revealed in centrifuge tests [11], the vibration of buried structures may be induced by two different mechanisms: namely the blast-induced stress wave and inertial loading. The blast-induced stress wave refers to the propagation of stress wave in soil media. This wave propagation may produce an impulse loading when confronting a buried structure. This impulse loading increases very fast (within 20 μs) and decreases within a short duration (80–120 μs). The inertial loading refers to the loading induced by the dynamical motion of soil mass in the surrounding of the explosive. This inertial loading develops over a relatively longer time and occurs after the propagation of stress wave. For such a problem, extra protection can be designed to attenuate the stress wave or to insulate the inertia of soil mass. So far, there are limited theoretical understandings for these two mechanisms.

A good deal of research has been experimentally carried out in the past few decades to study the vibration-screening problem. For example, Barkan [6] and McNeill et al. [7] were the first to report on the practical cases of vibration isolation. Barkan presented some field test results and suggested some guidelines for wave-barrier design. Particularly, Woods [8] systematically performed a series of field experiments on vibration screening by installing open trenches very close to the wave source (known as active isolation due to the wave barrier being placed close to the source), as well as in the far field of the wave source (known as passive isolation due to the wave barrier being placed close to the receiver building but far away from the wave source). In the near field, body waves are prominent but in the far field, the Rayleigh wave is dominant. Based on his experimental findings, Woods presented some critical relationships of normalized dimensions of an open trench. His results showed that a ground amplitude reduction of 75% or more was achievable. Haupt [9] carried out a series of model scale tests on the vibration isolation of various measures in a laboratory ground. He experimentally investigated solid barriers e.g. concrete core walls and lightweight barriers such as rows of bore holes and open trenches. He found that the screening effect of these barriers was a function of characteristic parameters in expression of wavelength-normalized dimensions. It was noted that wave sources in the above-mentioned experiments were all produced by mechanical vibrators in either vertical or horizontal directions. For the isolation of buried blast-induced ground shock, Davies [10,11] carried out a series of 20-g centrifuge tests to investigate the screening effect of geofoam barrier, concrete wall and their composites on the nearby buried structures. His centrifuge test results indicated that barriers containing low acoustic materials were highly effective in the attenuation of stress wave propagation. A well-designed wave barrier can largely reduce the magnitude of ground shock loading on buried structures.

The wave-barrier problems for underground explosion have been numerically and theoretically investigated too. For example, Aviles and Sanchez-Sesma [12] theoretically studied the foundation isolation from vibrations using solid piles as wave barriers. They achieved two closed-form analytical solutions: The exact solution of incident-plane SV waves was for a two-dimensional model which was formed with piles of infinite length and circular cross section that were embedded in an elastic, homogeneous, and isotropic unbounded space. Furthermore, an approximate solution of incident-plane Rayleigh waves was obtained for a three-dimensional model which was formed with piles of finite length and circular cross section that were embedded in an elastic, homogeneous, and isotropic half-space. Closed-form solutions are perfect but difficult to obtain. Numerical method is an alternative. Beskos and his colleagues developed a boundary element method (BEM) to investigate the vibration isolation of surface waves in both homogeneous and layered soils [13]. Al-Hussaini and Ahmad [14] conducted an extensive numerical study on the screening efficiency of a rectangular barrier by using their higher-order boundary element algorithm. They found that open (air) trenches, in-filled (concrete or bentonite) barriers, sheet pile walls, or even rows of piles can be effective wave barriers. However, their vibration source was input through a regular wave instead of blast loading. FEM has been employed to study the wave-barrier effect in the ground. For example, Haupt studied the effect of a solid barrier such as concrete wall with FEM and his numerical results were compared with small-scale laboratory tests where their loading source was still sine wave generated by a heavy machine [15]. Al-Hussaini et al. [16] compared the BEM results with experimental data available from public literatures. Gao et al. [17] presented an integral equation governing Rayleigh wave scattering. They theoretically studied the efficiency of ground vibration isolation through multi-rows of piles as passive barrier in a three-dimensional context. Hung and Ni [18] presented a

multiple neural networks model to estimate the screening effect of surface waves by in-filled trenches. Woods [19] summarized the latest development of the vibration screening with wave barriers since his early paper in 1968 [8]. He mentioned some new developments of wave barriers such as an air-cushion or air-bag system [20], a hollow pile system [21], and a honeycomb wave impeding barrier [33].

So far, few studies have been performed on the attenuation and diffraction of blast-induced stress waves through geofoam inclusions and lightweight fill materials although expanded polystyrene (EPS) geofoam blocks were successfully used as fillings in road constructions [22–24]. Geofoam is a lightweight polymeric material made by expansion of raw plastic beads. When expanded, beads become spherical shaped particles and each contains closed hollow cells in which air is trapped. The variation of its density largely depends on the fabrication process (current available density is 12–32 kg/m^3). EPS geofoam may have two functions for the attenuation of stress-waves. First, the less mass has less inertial force when subjected to blasting load. This geofoam layer may result in high gradient of particle velocity, producing a difference of particle velocity at its both sides. Second, high-damping properties of EPS geofoam can absorb blasting energy.

In this paper, the effects of soft porous layer barriers (open trench, inundated water trench, geofoam barrier, and concrete wall) on the reduction of buried blast-induced ground shock are numerically studied through commercial software package, LS-DYNA [25]. For convenience, this numerical model is set up based on the prototype dimension of the centrifuge test carried out by Davies [11]. That is, the numerical model is set up with two steel boxes symmetrically buried at both sides of the charge. One box is directly located in soil mass without protection (unprotected) and the other is located behind a soft porous layer barrier (protected). The soft porous layer barriers to be studied include an open trench, an inundated water trench and three in-filled geofoam layers with different densities, and a concrete wall. In the numerical model, the mechanical behaviors of soil media are described by an elastoplastic constitutive model for soil and crushable material. LS-DYNA is employed to implement the numerical simulations on the strain and acceleration of buried structures. The numerical results are evaluated by comparing their differences in protected and unprotected structures. These simulations show that both open trench and geofoam barriers can effectively reduce blast-induced stress waves. However, the inundated water trench and the concrete wall have almost no effect on the reduction of ground shock. This paper is organized as follows: Section 2 briefs the three-dimensional FEM model; Section 3 presents the constitutive models of soil, steel plate, concrete, geofoam, and water. Section 4 presents the numerical results. Section 5 draws the understanding and conclusion.

2. Finite element model

The prototype dimension of the centrifuge model tested by Davies [11] under 20-g is used for our numerical simulation. Prototype dimensions will be reduced to 1:n if the centrifuge test is running in n-g. As 20-g was used in centrifuge test, the dimension of centrifuge model is reduced to 1:20. Thus, the diameter of 75 cm in centrifuge model corresponds to the diameter of 15 m in the prototype dimension. For convenience, the prototype dimension is shown in Fig. 1a for bird view and b for section view. This model has one symmetry plane (see Fig. 1a) which is shown in Fig. 1b. This is a three-dimensional cylindrical model which has 15 m in diameter and 8.4 m in depth. The charge of 16 kg explosive is buried at a depth of 2 m from ground surface (free surface) along the central axis. A protection barrier of 0.24 m thick is placed 3 m away from the charge. This barrier may be an open trench, an inundated water trench, a concrete wall, one of three geofoam walls with different densities. Two cubical steel boxes representing two buried structures are symmetrically buried at the both sides of the charge. One is located behind a protection barrier which is called as the 'protected' structure. The other is symmetrically located at the same distance from the charge. This control specimen is denoted by the 'unprotected' structure. These two boxes are filled with the surrounding soil. Each box has its internal dimension of 1.8 m × 1.8 m × 1.8 m. The steel plate at the front face to charge has 0.5 mm in thickness. The back face steel plate is 2 mm thick and the side walls are 5 mm thick.

Arbitrary Lagrange–Euler (ALE) algorithm in LS-DYNA is employed in the simulation. The ALE algorithm has the capability of treating excessive deformation of elements [25]. The detail of FE mesh is shown in Fig. 1c, in which the steel boxes are discretized by 4-node shell elements and other parts are discretized by 8-node solid elements. Total approximate 160,000 solid elements and 1360 shell elements are used in the computation. In order to capture violent change of stress waves from blasting source, each surface of

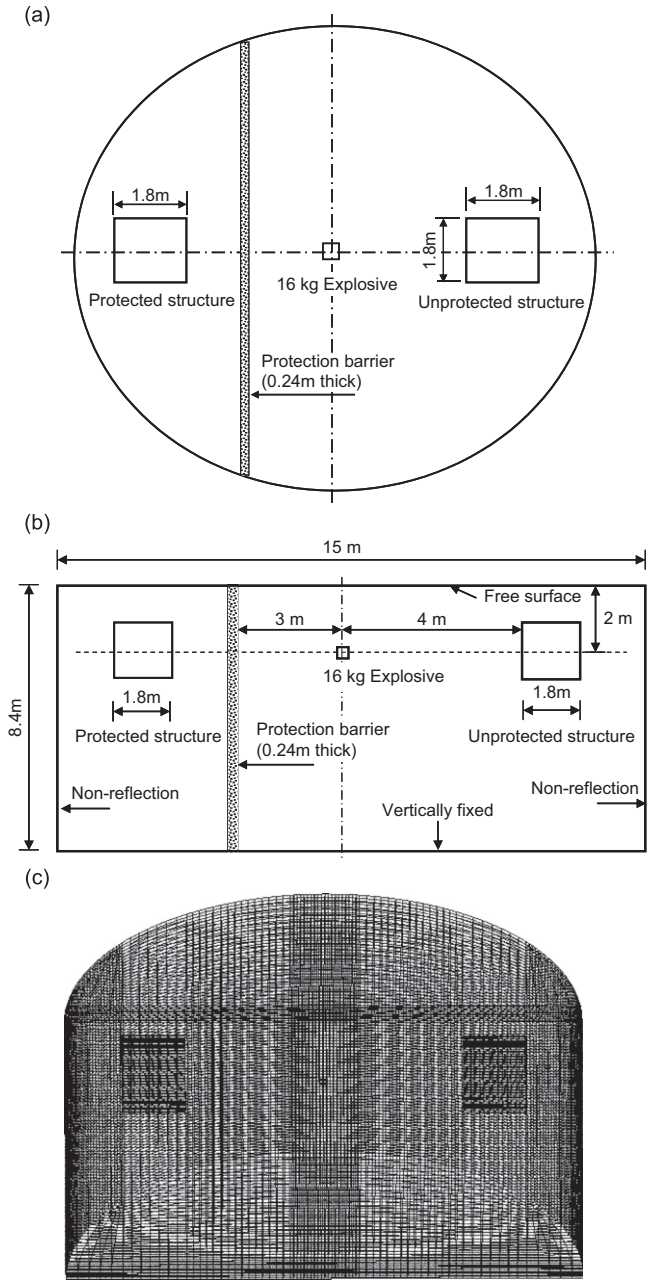

Fig. 1. Problem dimensions and FEM mesh: (a) typical plane view, (b) section along symmetrical plane, and (c) three-dimensional FEM mesh.

structures in the direction of blasting source is discretized into 200 shell elements. The dimension of each solid element ranges from 10 to 30 cm to adapt the variation of the frequency of stress waves in different locations. This numerical model has following boundary conditions: Vertical displacements at the bottom are fixed to restrain rigid body movement. Symmetrical boundary is applied to all horizontal displacements along the symmetry plane. The top surface is free surface which can reflect the stress waves. In order to be consistent to the centrifuge test where polystyrene sheet was used to absorb the stress waves at the model boundaries, the sides are set as non-reflecting or transmitting boundaries through applying following viscous normal and shear

stresses to the boundary segments [34]:

$$\sigma_n = -c_1 \rho V_p \dot{u}_n$$
$$\tau = -c_2 \rho V_s \dot{u}_t \tag{1}$$

where ρ, V_p, V_s are the material density, the dilatational (pressure) wave speed, and the shear wave speed of the transmitting media, respectively. $\dot{u}_n, \dot{u}_t$ are the particle velocities in the normal and tangential directions. c_1,c_2 are relaxation coefficients that have been introduced in order to improve the efficiency of the absorption. When the pressure waves only strike the boundary perpendicularly, relaxation is redundant ($c_1 = c_2 = 1$). However, the damping effect is not sufficient without relaxation if the shear waves are presented. Generally, the use of $c_1 = 1$ and $c_2 = 0.25$ results in a reasonable absorption of waves at the boundary although this cannot guarantee the full absorption of shear waves on the boundary. It is noted that LS-DYNA computes an impedance matching function (see discussion in Section 4.2) for all non-reflecting boundary segments based on an assumption of linear material behavior. Thus, the finite element mesh should be constructed so that all significant nonlinear behavior is contained within the discrete analysis model.

3. Constitutive models in computation

There are six materials in this numerical model: explosive, soil, geofoam, steel, concrete, air, and water. Their constitutive models are, respectively, stated as below.

3.1. JWL equation of state for explosive

Blasting event has two processes: The explosive detonation process and the development of the detonation product gas. The explosive detonation process can be described by a detonation velocity D and a Chapman–Jouget pressure P_{cj} according to the algorithm proposed by Giroux [35]. The development of the detonation product gas is modeled by the *Jones–Wilkens–Lee* (JWL) equation of state. This equation is widely used to model the pressure within the detonation product gas. This pressure p is expressed as

$$p = A\left(1 - \frac{\omega}{R_1 V}\right)e^{-R_1 V} + B\left(1 - \frac{\omega}{R_2 V}\right)e^{-R_2 V} + \frac{\omega E_0}{V} \tag{2}$$

A, B, R_1, R_2 and ω are material constants. V is the relative volume of detonation product and E_0 is the internal energy per initial volume. This paper uses 16 kg emulsion explosive in simulation, whose parameters are listed in Table 1.

3.2. Constitutive model for soil and crushable EPS geofoam

This model proposed by Krieg [26] is used for simple description of soil and crushable EPS geofoam. If yield stress is too low, this model can produce nearly fluid like behaviors. In this model, deviatoric behavior is governed by a pressure-dependent flow rule. Its yield function is

$$f = J_2 - (a_0 + a_1 p + a_2 p^2) \tag{3}$$

Table 1
Explosive parameters for JWL model

Density (kg/m^3)	D (m/s)	P_{cj} (GPa)	A (GPa)	B (GPa)	R_1	R_2	ω	E_0 (GPa)
1000	3600	21	47.6	0.529	3.5	0.9	1.3	4.5

where a_0, a_1 and a_2 are material constants, p is the hydrostatic pressure, and

$$J_2 = \frac{1}{2} S_{ij} S_{ij}, \quad S_{ij} = \sigma_{ij} - \delta_{ij} p, \quad p = \frac{1}{3} \sigma_{ii} \tag{4}$$

where σ_{ij} is the stress tensor, S_{ij} is the deviatoric stress tensor, δ_{ij} is the Kronecker delta.

The implementation of this model is straightforward. One history variable, the maximum volumetric strain in compression, is stored. If the new compressive volumetric strain exceeds the stored value, loading is indicated. When the yield condition is violated, the updated trial stresses, S_{ij}^*, are scaled back using a simple radial return algorithm:

$$S_{ij}^{n+1} = \left(\frac{a_0 + a_1 p + a_2 p^2}{J_2} \right)^{1/2} S_{ij}^* \tag{5}$$

The model parameters used in simulation are listed in Table 2 for soil and in Table 3 for EPS geofoam with the density of 12, 21, and 27 kg/m^3. It is noted that the deformation under hydrostatic compression is usually given by input tabulated data of hydrostatic pressure versus volumetric strain curve. For this clayey soil, the hydrostatic compression curve can be approximated using the following formula

$$p = p_0 e^{b\varepsilon_v^p} \tag{6}$$

where p_0 and b are material parameters. For this soil, the experimental fitting curve is obtained as $p = 8.626 \times 10^5 e^{18.94\varepsilon_v^p}$ (kPa). This formula is used to generate tabulated data for computation. For the EPS geofoam, the hydrostatic compression curve obtained from the experimental data [24] is listed in Table 3b.

Table 2
Soil parameters for crushable soil model

Density (kg/m^3)	Poisson's ratio	E (MPa)	G (MPa)	K (MPa)	a_0 (MPa)^2	a_1 (MPa)	a_1
1800	0.48	47.36	16.0	394.7	2.4e−6	0.0136	0.1232

Table 3
(a) Geofoam parameters for crushable foam model and (b) tabulated data of hydrostatic pressure versus volumetric strain of EPS geofoam

(a)

Density (kg/m^3)	P_c (kPa)	G (MPa)	K (MPa)	a_0(kPa)^2	a_1(kPa)	a_2
12.00	−12	1.22	0.61	529.0	3.220	0.005
21.00	−27	2.12	1.13	2246.8	10.428	0.0121
27.00	−42	2.92	1.62	5535.36	8.928	0.0036

(b)

Hydrostatic pressure (kPa)				Volumetric strain			
Pressure	$\rho_0 = 27$ kg/m^3	$\rho_0 = 21$ kg/m^3	$\rho_0 = 12$ kg/m^3	Strain	$\rho_0 = 27$ kg/m^3	$\rho_0 = 21$ kg/m^3	$\rho_0 = 12$ kg/m^3
p_1	0.000	0.000	0.000	ε_1	0.0000	0.0000	0.0000
p_2	4.918	10.000	9.689	ε_2	−0.0053	−0.0123	−0.0201
p_3	10.109	14.286	14.879	ε_3	−0.0113	−0.0165	−0.0319
p_4	24.863	39.895	20.069	ε_4	−0.0207	−0.0328	−0.0458
p_5	42.721	51.286	24.567	ε_5	−0.0340	−0.0488	−0.0632
p_6	68.306	61.429	29.066	ε_6	−0.0475	−0.0645	−0.0820
p_7	84.973	65.714	34.602	ε_7	−0.0648	−0.0800	−0.1110
p_8	95.082	70.000	39.792	ε_8	−0.0859	−0.0953	−0.1332
p_9	101.634	74.286	47.405	ε_9	−0.1090	−0.1178	−0.1706
p_{10}	104.645	81.429	49.481	ε_{10}	−0.1296	−0.1398	−0.1815

(i) Pressure is positive when in compression.
(ii) The strain is the natural logarithm of the relative volume and is negative in compression.

A cutoff value of hydrostatic tension is used for tensile failure. If hydrostatic tension exceeds its cutoff value, the hydrostatic pressure is set to be the cutoff value. At this time, the deviatoric stress tensor is set as zero.

3.3. Constitutive model for steel

An elastoplastic model with either isotropic hardening, kinematic hardening, or their combination [27] is used here to describe the mechanical behaviors of steel. In this model, the yield function is

$$f = \frac{1}{2}\xi_{ij}\xi_{ij} - \frac{1}{3}\sigma_y^2 = 0 \tag{7}$$

where

$$\xi_{ij} = S_{ij} - \alpha_{ij} \tag{8}$$

where α_{ij} has the co-rotational rate as

$$\alpha_{ij}^{\nabla} = (1-\beta)\frac{2}{3}E_p\dot{\varepsilon}_{ij}^p \tag{9}$$

if the strain rate is accounted for, the yield stress can be expressed as

$$\sigma_y = [1 + (C\dot{\varepsilon})^{\eta}](\sigma_0 + \beta E_p \varepsilon_{\text{eff}}^p) \tag{10}$$

where C, η, and β are the constants, and $0 \leqslant \beta \leqslant 1$. $\varepsilon_{\text{eff}}^p = \int_0^t (\frac{2}{3}\dot{\varepsilon}_{ij}^p \dot{\varepsilon}_{ij}^p)^{1/2}\,\mathrm{d}t$ is the equivalent plastic strain, $\dot{\varepsilon} = \sqrt{\dot{\varepsilon}_{ij}\dot{\varepsilon}_{ij}}$ is the strain rate; σ_0 is the initial yield strength. It is noted that the plastic strain rate is the difference between the total and the elastic strain rates as:

$$\dot{\varepsilon}_{ij}^p = \dot{\varepsilon}_{ij} - \dot{\varepsilon}_{ij}^e \tag{11}$$

E_p is plastic hardening modulus which is

$$E_p = \frac{E_t E}{E - E_t} \tag{12}$$

where E_t is the tangential modulus. The material parameters of normal low-mild steel used herein are listed in Table 4.

3.4. Constitutive model for concrete

The mechanical behavior of concrete is described by a compression-hardening constitutive model. As concrete has different mechanical properties when subjected to loadings in compression and tension, its yield function can be found to have different forms. If the loading is in compression, the deviatoric perfectly plastic yield function is

$$f = \sqrt{3J_2} - F_1(p) = \sigma_y - F_1(p) \tag{13}$$

This is a pressure dependent yield function and $F_1(p)$ expresses the pressure-dependent properties of concrete under compression.

If the loading is in tension, the yield function is

$$f = \sqrt{3J_2} - F_2(p) \tag{14}$$

Table 4
Steel parameters for plastic kinematic hardening model

Density (kg/m^3)	E (MPa)	Poisson's ratio	σ_0 (MPa)	E_t (MPa)	β	C
7830	2.07×10^5	0.3	500	20.7	0.0	0.0

The $F_1(p)$ and $F_2(p)$ can be expressed in tabulated data and are directly input into the LS-DYNA. Further, pressure versus volumetric strain gives a hardening rule of concrete. These functions can be used to describe the compressibility of concrete under different loading paths. As an example, fundamental parameters of a concrete used in our computation are listed in Table 5a. This concrete has a tabulated hardening rule (see Table 5b) and a tabulated yield function (see Table 5c) for compression.

The mechanical properties of concrete will be degraded with crack development. The current yield stress σ_y^* is expressed as $\sigma_y^* = r\sigma_y$ due to the invoking of cracking after strain ε_1^p. This factor r is decreasing with an increase in the accumulated plastic strain and approaching to a residual value b which corresponds to the residual strength of concrete. The strain where r reaches the residual value b is known as ε_2^p. In another words, $r = f(\varepsilon^p) \subset (1,b)$ when plastic strain $\varepsilon^p$is between ε_1^p and ε_2^p. The ε_1^p and ε_2^p are functions of hydrostatic pressure p. For the concrete used in our computation, the strain ε_1^p versus (hydrostatic) pressure is tabulated in Table 5d

Table 5a
Concrete parameters for damage model

Density (kg/m^3)	E (MPa)	Poisson's ratio	p_c (MPa)	B
2400	3.0×10^4	0.2	−2	0.3

Table 5b
Curve for pressure versus volumetric strain

Pressure p (GPa)	Volumetric strain ε_v
0.0	0.0
9.53	0.0230
18.23	0.0650
26.24	0.1300
33.65	0.1750
40.55	0.2250
47.00	0.3500

Table 5c
Curve for von Mises stress versus pressure

Stress σ_y (GPa)	Pressure p (GPa)
0.0	0.0
0.400	0.240
0.800	0.550
1.200	0.950
1.400	1.260
1.800	1.550
10.00	15.50

Table 5d
Curve plastic strain versus pressure at which fracture begins

Plastic strain ε_1^p	Pressure p (GPa)
0.00	0.00
0.00015	1.00
0.001	4.00
0.010	49.0
0.100	490.0

Table 5e
Plastic strain at which residual strength is reached versus pressure

Plastic strain ε_2^p	Pressure p (GPa)
0.00	1.00
0.00015	2.00
0.001	5.00
0.010	50.0
0.100	500.0

and the strain ε_2^p versus pressure is tabulated in Table 5e. Both curves are hardly different due to the brittleness of the concrete. In addition, concrete cannot resist any shear force as well as additional pressure when tensile pressure drops below the cutoff value p_c.

3.5. Equation of state for air and water

The Gruneisen equation of state is employed to describe the behaviors of air and water. Water is modeled as a compressible fluid. For its compression, the equation of state is

$$p = \frac{\rho_0 k^2 \mu \left[1 + \left(1 - \frac{\gamma_0}{2}\right)\mu - \frac{\alpha}{2}\mu^2\right]}{\left[1 - (S_1 - 1)\mu - S_2\frac{\mu^2}{\mu+1} - S_3\frac{\mu^3}{(\mu+1)^2}\right]^2} + (\gamma_0 + \alpha\mu)E_0 \tag{15}$$

For the expansion of air, the equation of state can be expressed as

$$p = \rho_0 k^2 \mu + (\gamma_0 + \alpha\mu)E_0 \tag{16}$$

where the excess compression μ

$$\mu = \frac{\rho}{\rho_0} - 1 \tag{17}$$

In addition, k is the speed of sound; S_1, S_2, and S_3 are fitting coefficients; γ_0 is the Gruneisen gamma; α is the first-order volume correction coefficient. For our computation, main material parameters are listed in Table 6 for air and Table 7 for water. The internal energy per initial volume and the initial volume are taken as defaults in LS-DYNA.

4. Computational schemes and results analysis

Four schemes of protection barriers are numerically investigated: an open trench, an inundated water trench, three in-filled geofoam walls (with density of 12, 21, and 27 kg/m^3), and a concrete wall. Numerical results are presented in the subsequent context.

4.1. Response of buried structures

Two indices, effective strain and acceleration of buried structures can be used to measure the effectiveness of protection barriers on the reduction of ground shock. As the buried structures are made of steel, its tensile strain is regarded as positive. The effective strain on the mid surface of two buried structures facing to the explosive is taken as one index for the evaluation of ground shock pressure. The acceleration at the same point is taken as another index to measure the effectiveness of protection barriers on vibration control. In this presentation, the structure behind the protection barrier is known as ‘protected’ and the controlled one without protection barrier is known as ‘unprotected’. The effectiveness of protection barriers is measured by the difference in their responses.

Table 6
Air parameters for Gruneisen equation of state

Density (kg/m^3)	k (10^3 m/s)	γ_0	α
1.25	0.344	1.4	0.0

Table 7
Water parameters for Gruneisen equation of state

Density (kg/m^3)	k (10^3 m/s)	γ_0	S_1	S_2	S_3	α
1000	1.65	0.35	1.92	−0.096	0	0.0

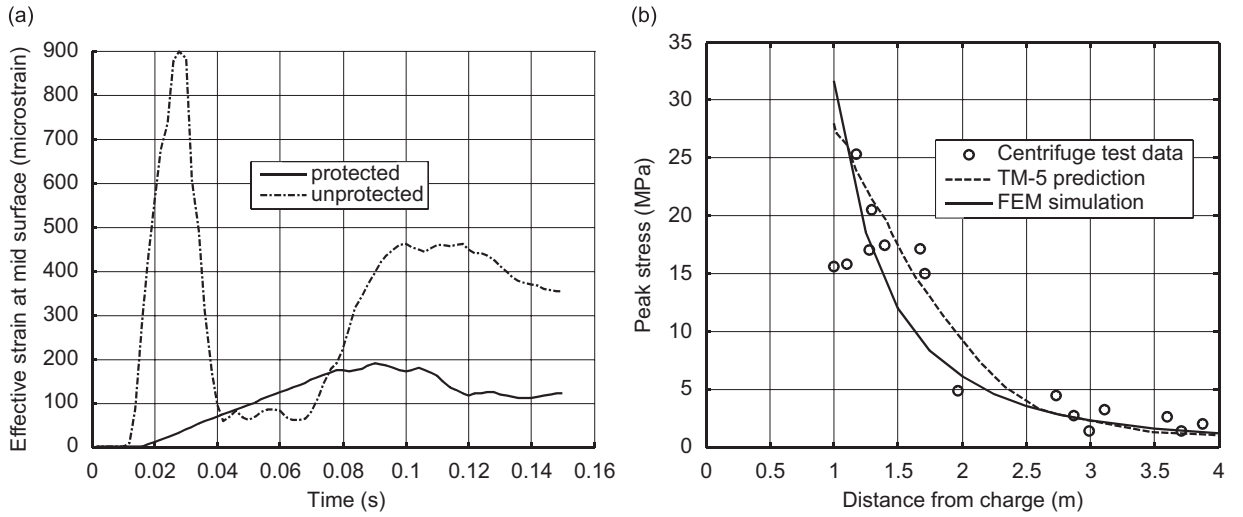

Fig. 2. Typical comparison for ground shock propagations: (a) comparison of effective strain at mid surface of structures (open trench case) and (b) typical comparison of centrifuge test and FEM simulation at free-field side for polystyrene barrier case.

4.1.1. General properties of the responses

A typical response of effective strain is shown in Fig. 2a. The response at the unprotected structure has two distinct phases. In the first phase, the peak effective strain is quickly developed at around 0.03 s. After the peak, a continuous decrease is observed until some time after 0.04 s. In the second phase, another slow increase is observed in the development of effective strain after 0.08 s and the peak is much lower than that in the first phase. This phenomenon was observed in the centrifuge test by Davies [11], where the first phase was referred as stress wave propagation and the second phase was referred as inertial loading. In order to check the capability of the numerical model, Fig. 2b presents the typical comparison between centrifuge test and numerical simulation at free-field side for polystyrene barrier case when laboratory sand is used (density of 16.68 KN/m^3, seismic velocity of 500 m/s). TM-5 prediction done by Davies [11] is also plotted for comparison. This indicates that the current numerical simulation can give reasonable results.

4.1.2. Mesh convergence study

In order to validate the convergence of the numerical solution for the problem studied, mesh convergence studies were carried out for the open trench. Fig. 3 shows the results obtained for two meshes when concrete wall is used. Element length of the coarse mesh is almost twice of fine mesh (This fine mesh was used in finite element model as stated in Section 2). Their responses are almost identical at ground shock stage and have

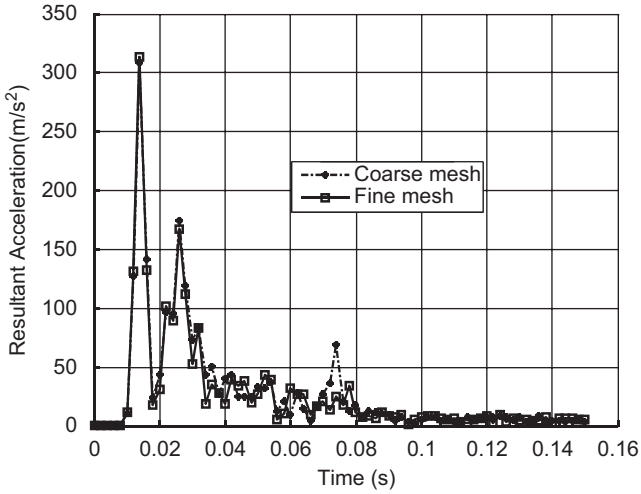

Fig. 3. Mesh convergence for concrete wall case.

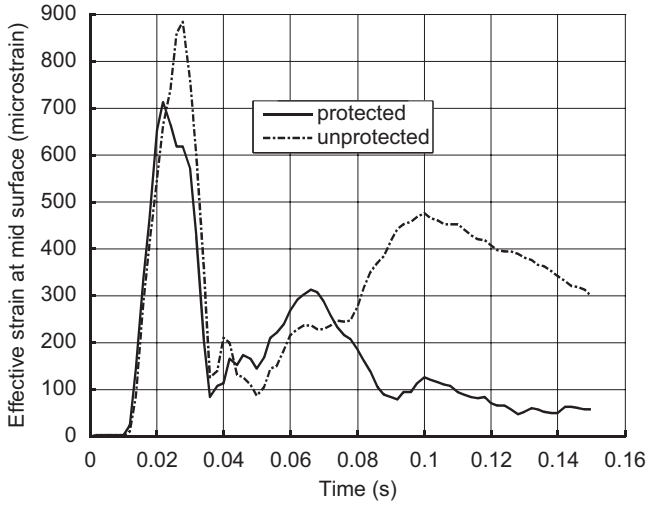

Fig. 4. Comparison of effective strain at mid surface of structures (inundated water trench).

little difference at inertial loading stage. Previous research indicated that element length should be smaller than one-half of the Rayleigh wavelength [16]. For explosion loading, the impulse loading is single peak. Estimated frequency is 100 Hz and estimated wave velocity of soil media is approximately 100–150 m/s. Therefore, the wavelength is 1.0–1.5 m. To ensure accuracy, element size should be kept at less than one eighth to one fifth of the shortest possible wavelength according to reference [28]. Therefore, our mesh used in computation is reasonable.

4.1.3. Reduction of effective strain by protection barriers

A substantial reduction of peak amplitude of effective strain is observed after the protection of an open trench. As shown in Fig. 2 a, the peak amplitude can be reduced by almost 80% with this open trench. This result is consistent to site observations [8,9] and theoretical analysis [14,29,30]. However, the protection of the open trench is largely weakened if the open trench is inundated with water. Fig. 4 shows that the simulation curves of effective strains on both protected and unprotected structures are similar. However, the inundated

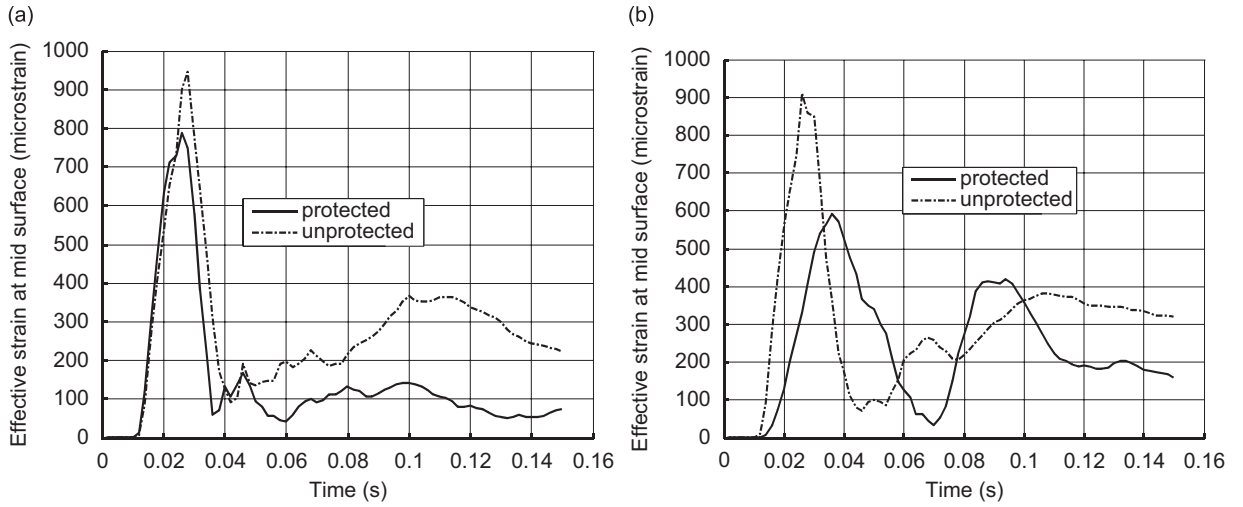

Fig. 5. Comparison of effective strain at mid surface of structures: (a) concrete wall and (b) geofoam barrier with density of 12 kg/m^3.

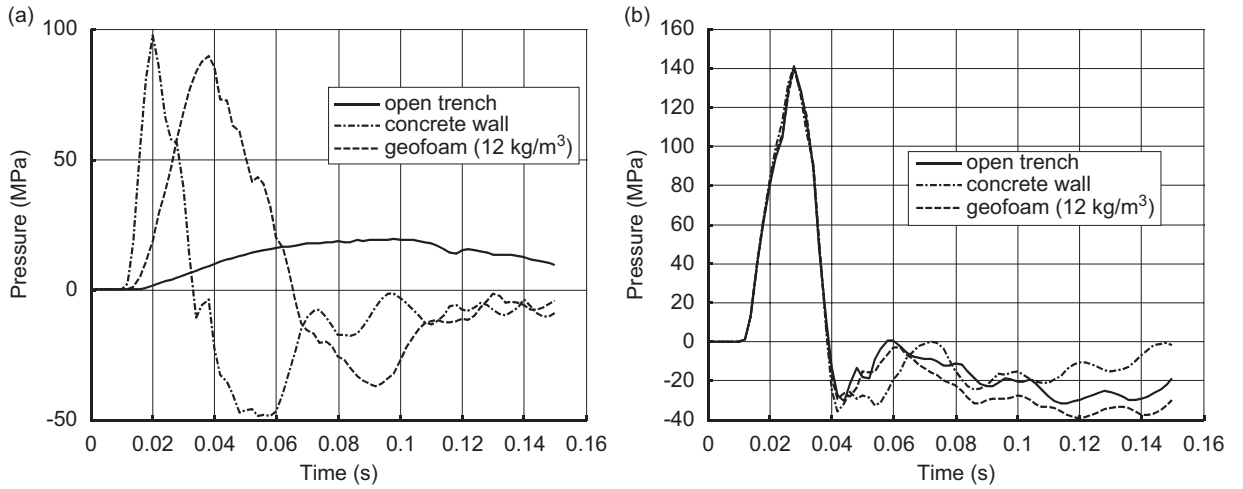

Fig. 6. Comparison of pressure on the mid surface of structures: (a) protected structure and (b) unprotected structure.

water trench can reduce a little strain in the first phase but much more in the second phase. As shown in Fig. 5a, the concrete wall is slightly effective in reducing the strain in the first phase but highly effective in reducing the strain in the second phase. In contrast, as shown in Fig. 5b, the geofoam barrier with the density of 12 kg/m^3 performs some effectiveness in reducing the strain in the first phase but little effectiveness in the attenuation of the strain development in the second phase.

As we know, the effective strain of structures may be caused by the propagation of normal stress (soil pressure) in soil media. For verification purpose, the pressure (hydrostatic stress) near the central point of this mid surface of structures is shown in Fig. 6. At the unprotected structure side, the same response of pressure for all protection barriers is observed in the first phase but a little difference is observed in the second phase. This figure verifies the correctness of the numerical simulation. At the protected structure side, the responses of pressure vary with protection barriers. Different protection barriers have different reductions of peak magnitude in both phases. The geofoam barrier with density of 12 kg/m^3 can reduce approximately 36% pressure in the first phase. This result is consistent to our field trial results where soil pressure after the

geofoam barrier was measured to be reduced from 36–43% for 5 t TNT surface explosion at the scale distance of approximately 2.0 m/kg$^{1/3}$ [31].

4.1.4. Accelerations of structures

The resultant acceleration histories at the mid surface of both structures are presented in Fig. 7. In both protected and unprotected structures, two distinct peaks are observed. In the first phase, the peak acceleration is developed at around 0.018 s when the stress wave arrives at these structures. After the first peak, the acceleration continuously decreases until approximately 0.023 s when the stress wave passes through the structures. In the second phase, the peak acceleration appears at around 0.04 s. The first peak of acceleration is highly attenuated by the open trench and the geofoam barriers. The unprotected acceleration is observed as 300 m/s^2. The acceleration at the protected structure is reduced to less than 10 m/s^2 for the open trench, to 32 m/s^2 for the geofoam barrier with density of 12 kg/m^3 to 54 m/s^2 for the geofoam barrier with density of 21 kg/m^3 and to 66 m/s^2 for the geofoam barrier of density of 27 kg/m^3. It is slightly reduced to 269 m/s^2 for the concrete wall and 231 m/s^2 for the inundated water trench. In the second phase, the attenuation on peak acceleration is still effective for the open trench but comparatively less effective for those geofoam barriers, from 169–91 m/s^2 for density of 12 kg/m^3, from 147–79 m/s^2 for density of 21 kg/m^{3}and from 130–88 m/s^2 for density of 27 kg/m^3. The screening effect is inconspicuous for both the inundated trench and the concreted wall.

4.2. Response of protection barriers

In order to measure the effectiveness of protection barriers, a reduction factor (RF) is defined as follows:

$$\mathrm{RF} = \frac{F_c - F_p}{F_c} \tag{18}$$

where F_c is the peak value of the control specimen and F_p being the corresponding peak value of the protected specimen. Here they are taken as strain /acceleration on the mid surface of the structures. Fig. 8a shows the variation of the RF with barrier materials in the first phase (ground shock stage). It is found that the reduction factor of the strain on the structure surface and the normal stress (pressure) are almost identical. The reduction factor is always larger for acceleration than for strain and pressure. For the in-filled trench with soft materials, their effectiveness ranks as: open trench > geofoam barriers (12, 21 and 27 kg/m^3) > inundated water trench > concrete wall. The open trench and geofoam barriers (with density of 12 kg/m^3) can reduce up

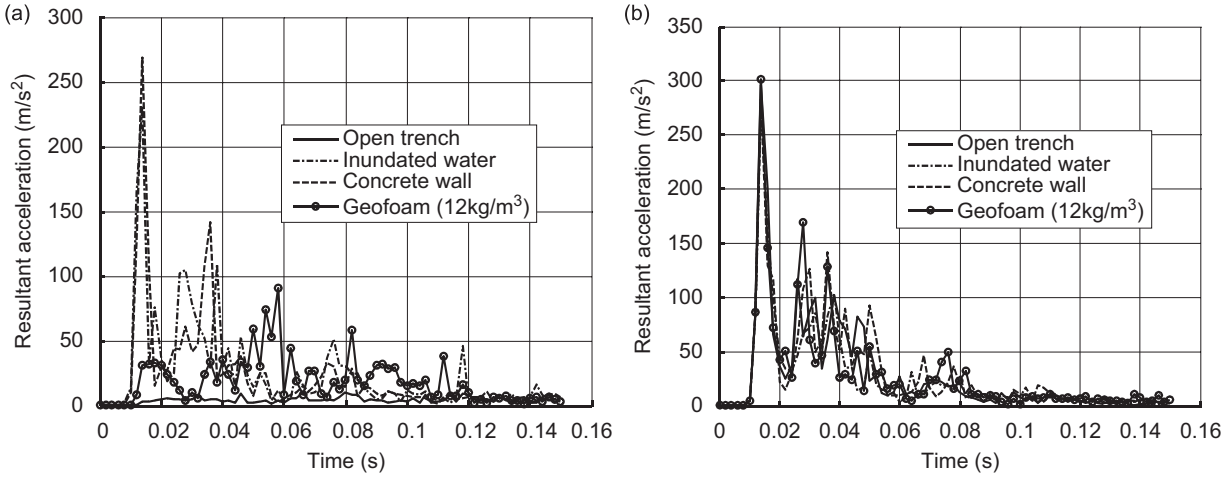

Fig. 7. Comparison of resultant acceleration on the mid surface of structures: (a) protected case and (b) unprotected case.

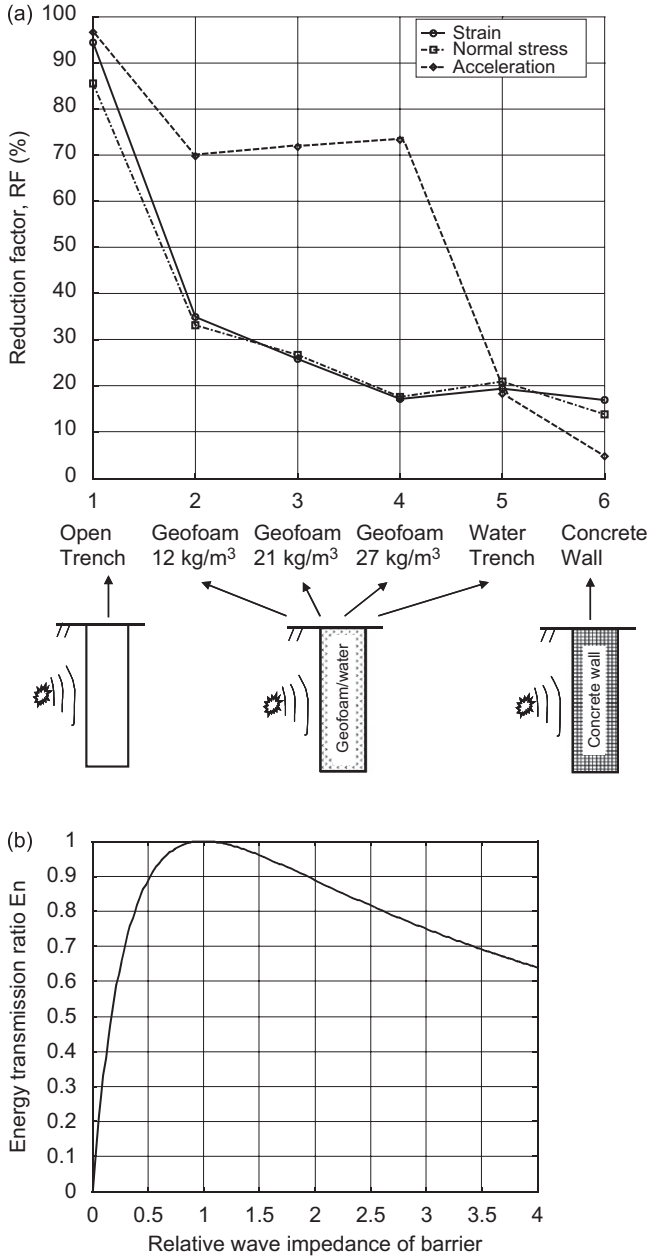

Fig. 8. Reduction factor in the ground shock stage: (a) reduction factor for different barriers and (b) energy transmission ratio with relative wave impedance.

to 70% for acceleration but approximate 30% for normal stress (soil pressure). The effectiveness of geofoam barriers on normal stress/strain varies with geofoam density, determining the wave impedance ratio of geofoam to surrounding soils.

The wave impedance is defined as

$$z = \rho V \tag{19}$$

Where ρ and V are the density and wave speed of the media.

The transmission and reflection of propagating waves through an interface of the soil (denoted as subscript 1) and the barrier material (denoted as subscript 2) depend on their impedance difference. An energy transmission coefficient through the interface can be expressed as

$$E_n = \frac{4Z_1Z_2}{(Z_1+Z_2)^2} = \frac{4Z_2/Z_1}{(1+Z_2/Z_1)^2} \tag{20}$$

This impedance difference or mismatch can be scaled by the relative wave impedance of barrier material, Z_2/Z_1. Fig. 8b shows the variation of energy transmission coefficient with the relative wave impedance. This figure shows that the energy transmission coefficient can be less than 1 if the relative wave impedance is different from 1. It is also noted that more energy is reflected from the interface of soil and soft barrier. That is, the isolation effect is high when the relative impedance of the barrier is low than 1. Therefore, soft barrier is more effective than hard barrier in screening effect.

The horizontal deformation facing to the explosive and the normal stress on the protection barrier surface are observed here. Fig. 9 is the comparison of horizontal deformations of both sides of the protection barriers at a time of 0.15 s. Fig. 9a is the comparison at the front surface and Fig. 9b is the comparison at the back surface. It can be seen that the front surface of the open trench has the biggest horizontal displacement possibly leading to localized collapse. On the back surface, large deformation is only observed at the top part. The inundated water trench has smaller deformation than the open trench but much larger deformation than other barriers. Fig. 10 compares the normal stresses on both surfaces of protection barriers at a time of 0.01 s. For the open trench and geofoam barriers, the normal stresses are much smaller than those of the concrete wall and the inundated water trench. Fig. 10b shows that this normal force is transferred to the back surface through either the concrete wall or the inundated water trench, but this normal force cannot be effectively transferred to the back through the open trench. In addition, the geofoam barrier can transfer partial normal force to the back. Therefore, the force at either front or back surface is much larger for concrete wall and inundated water trench. Geofoam and open trench have much less forces at the front surface and the back surface.

4.3. Mechanism analysis

Two distinct phases are observed in both effective strain and acceleration histories. This indicates that two distinct loading mechanisms may contribute to the responses of the buried structures at different time scales: ground shock impact and inertial loading. Different protection barriers have different performances for these two loading mechanisms.

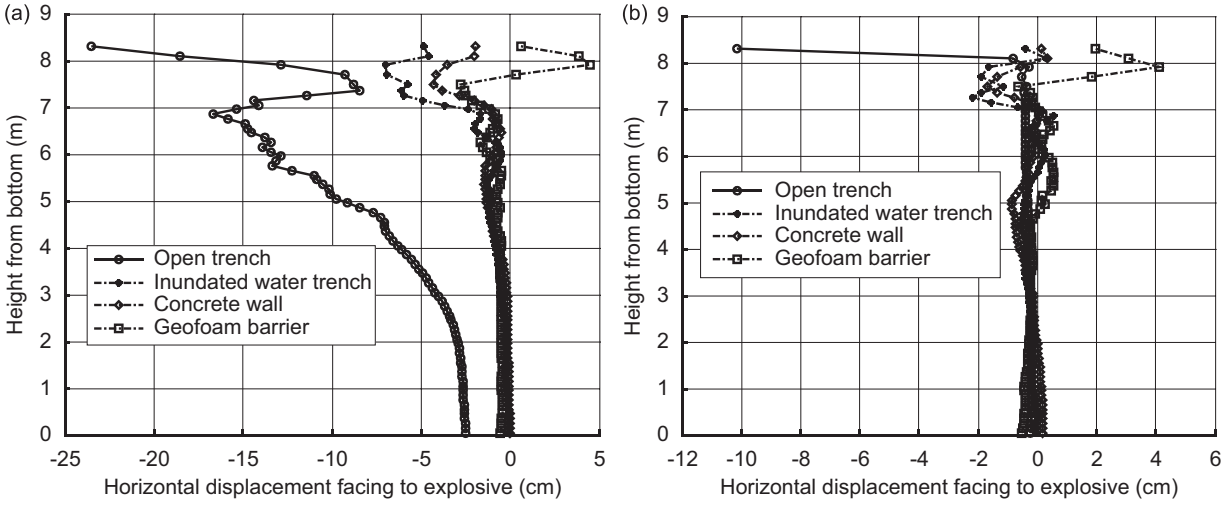

Fig. 9. Deformations of protection barriers at time of 0.15 s: (a) at front surface and (b) at back surface.

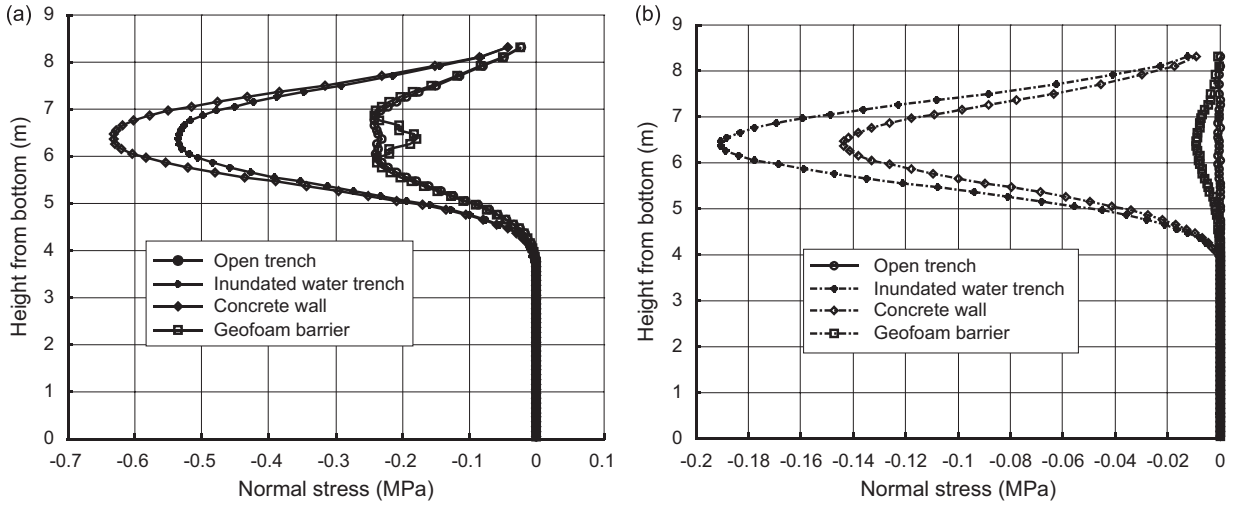

Fig. 10. Normal stresses of protection barriers at time of 0.01 s: (a) at front surface and (b) at back surface.

Although open trench is highly effective in reducing the strain wave and in attenuating the oscillation response of structures [8,14,19,32], the open trench after inundated water facilitates much larger transmission of normal stress. It becomes almost ineffective in resisting stress wave. This suggests that open trench may not be the best practical protection measures, particularly in the heavily raining area.

Furthermore, concrete wall is an effective barrier in reducing the effective strain in the second phase due to its great bending stiffness. It can effectively transfer the interaction force between soil and buried structure when subjected to blast-induced dynamic loadings. Thus the concrete wall can only provide a limited vibration screening on the propagation of ground shock in soil media. In contrast, geofoam barriers are limited in reducing the strain wave in the second phase due to the dynamic soil-structure interaction; it does significantly reduce much larger magnitude of vibrations in the protected structure than in the unprotected structure in the ground shock phase. It is also noted that its effectiveness in the reduction of ground shock varies with the density of the geofoam (wave speed is also associated with density). More exactly, the reduction factor depends on the relative wave impedance to surrounding media or impedance mismatch.

5. Conclusion

A structure-soil-blast-protection barrier interaction analysis is carried out to investigate the protective effectiveness of open trench, inundated trench, geofoam barrier and concrete wall. The pressure and acceleration of buried structures, the deformation and normal stress of the barriers are compared and evaluated. From these studies, the following understandings and conclusions can be made:

First, the most effective barrier for the blast-induced stress wave propagation is open trench. However, its protection effectiveness is largely weakened if the trench is inundated with water. The protected and unprotected structures have almost identical peak strains and accelerations for inundated water trench even if trench collapse is not considered. Therefore, open trench is not a good choice as a permanent protection barrier in practice. Open trenches are also susceptible to localized collapse and could lead to long-term maintenance issues.

Second, concrete wall can effectively resist the inertial loading but cannot effectively reduce the ground shock impact. In the ground shock stage, the vibration can be reduced up to 10% in acceleration and less than 20% in normal stress and strain in our computation. However, it has capability to screen the response of buried structures due to inertial loadings.

Third, geofoam barriers perform well in reducing the blast-induced stress waves. Furthermore, the geofoam barriers with different densities are of variable performances in the stress wave reduction. In engineering, the geofoam barrier is designable, thus being more practicable as a permanent protection layer.

It is noted that the current model does not describe the inertial loading due to blast-induced crater well. The numerical simulation on the inertial loading needs to be improved in the future, including the blast-induced upheave of soil mass around protection barriers. The shape of a protection barrier has an influence on its screen effect [36]. However, this paper only investigated the screening effect of wave barriers with plane interface. The effect of curved interfaces of wave barriers should be further investigated.

References

[1] H.H. Hung, J. Kuo, Y.B. Yang, Reduction of train-induced vibrations on adjacent buildings, *Structural Engineering and Mechanics* 11 (5) (2001) 503–518.
[2] L. Anderesn, S.R.K. Nielsen, Reduction of ground vibration by means of barriers or soil improvement along a railway track, *Soil Dynamics and Earthquake Engineering* 25 (2005) 701–716.
[3] Z.L. Wang, Y.C. Li, J.G. Wang, Numerical analysis of attenuation effect of EPS geofoam on stress-waves in civil defense engineering, *Geotextiles and Geomembranes* 24 (2006) 265–273.
[4] C. Comina, S. Foti, Surface wave tests for vibration mitigation studies, *Journal of Geotechnical and Geoenvironmental Engineering—ASCE* 133 (1) (2007) 1320–1324.
[5] R.K. Shrivastava, N.S.V. Kameswara Rao, Response of soil media due to impulse loads and isolation using trenches, *Soil Dynamics and Earthquake Engineering* 22 (2002) 695–702.
[6] D.D. Barkan, *Dynamics of Bases and Foundations*, McGraw-Hill, New York, NY, 1962.
[7] R.L. McNeill, B.E. Margason, F.M. Babcock, The role of soil dynamics in the design of stable test pads, *Proceedings of the Guidance and Control Conference*, 1965, pp. 366–375.
[8] R.D. Woods, Screening of surface waves in soils, *Journal of Soil Mechanics and Foundation Division—ASCE* 94 (4) (1968) 951–979.
[9] W.A. Haupt, Model tests on screening of surface waves, *Proceedings of the 10th Conference on Soil Mechanics and Foundation Engineering*, Vol. 3, Stockholm, 1981, pp. 215–222.
[10] M.C.R. Davies, Modelling of dynamic soil structure interaction resulting from impulsive surface loading, H.-Y. Ko, F.G. Mclean (Eds.), *Proceedings of the International Conference on Centrifuge*, Colorado, Balkema, 1991, pp. 487–493.
[11] M.C.R. Davies, Dynamic soil structure interaction resulting from blast loading, in: Leung, Lee, Tan (Eds.), *Centrifuge94*, Balkema, Rotterdam, 1994, pp. 319–324.
[12] J. Aviles, F.J. Sanchez-Sesma, Foundation isolation from vibrations using piles as barriers, *Journal of Engineering Mechanics ASCE* 114 (11) (1988) 1854–1870.
[13] D.E. Beskos, B. Dasgupta, I.G. Vardoulakis, Vibration isolation using open or filled trenches, Part 1: 2-D homogeneous soil, *Computational Mechanics* 1 (1986) 43–63.
[14] T.M. Al-Hussaini, S. Ahmad, Design of wave barriers for reduction of horizontal ground vibration, *Journal of Geotechnical Engineering, ASCE* 117 (4) (1991) 616–639.
[15] W.A. Haupt, Isolation of vibration by concrete core walls, *Proceedings of the Ninth International Conference on Soil mechanics and Foundation Engineering*, Vol. 2, Japanese Society of Soil mechanics and Foundation Engineering, 1977, pp. 251–256.
[16] T.M. Al-Hussaini, S. Ahmad, J.M. Baker, Numerical and experimental studies on vibration screening by open and in-filled trench barriers, in: S. Chouw (Ed.), *Wave 2000*, Balkema, Rotterdam, 2000, pp. 241–250.
[17] G.Y. Gao, Z.Y. Li, Ch Qiu, Z.Q. Yue, Three-dimensional analysis of rows of piles as passive barriers for ground vibration isolation, *Soil Dynamics and Earthquake Engineering* 26 (2006) 1015–1027.
[18] C.C. Hung, S.H. Ni, Using multiple neural networks to estimate the screening effect of surface waves by in-filled trenches, *Computers and Geotechnics* 34 (2007) 397–409.
[19] R.D. Woods, Vibration screening with wave barriers, in: S. Wu, W. Zhang, R.D. Woods (Eds.), *A Look Back for Future Geotechnics*, Balkema, 2001, pp. 325–348.
[20] K.R. Massarsch, Ground vibration isolation using gas cushions, *Proceeding of the Second International Conference on Recent Advances in Geotechnical Earthquake Engineering and Soil Dynamics*, St. Louis, Missouri, March 11–15, 2001, pp. 1461–1470.
[21] K. Hayakawa, Y. Kani, N. Matsubara, T. Matsui, R.D. Woods, Ground vibrations isolation by PC wall-piles. *Proceedings of the Fourth International Conference on Case Histories in Geotechical Engineering*, St. Louis, MO, March 1997, pp. 672–677.
[22] J.S. Horvath, The compressive inclusion function of EPS geofoam, *Geotextiles and Geomembranes* 15 (1997) 77–120.
[23] J.S. Horvath, *Cellular geosynthetics in transportation applications*, Geotechnical Special Publication 126, 2004, pp. 627–636.
[24] Y. Zou, C.H. Leo, Laboratory studies on engineering properties of expanded polystyrene (EPS) material for geotechnical applications, *Second International Conference on Ground Improvement Techniques*, Singapore, 1998, pp. 581–588.
[25] J.O. Hallquist, *Theoretical manual of LS-DYNA3D (V.960)*, Livermore Software Technology Corp, USA, 1998, pp. 3.1–4.1.
[26] R.D. Krieg, A simple constitutive description for cellular concrete, Sandia National Laboratories, Albuquerque, NM, Report No: SC-DR-72–0883, 1972.
[27] R.D. Krieg, S.W. Key, Implementation of a time dependent plasticity theory into structural computer programs, *Constitutive Equations in Viscoplasticity: Computational and Engineering Aspects—ASME* 20 (1976) 125–137.
[28] M.H. EI Naggar, A.G. Chehab, Vibration barriers for shock-producing equipment, *Canadian Geotechnical Journal* 42 (2005) 297–306.

[29] S.E. Kattis, D. Polyzos, D.E. Besko, Modelling of pile wave barriers by effective trenches and their screening effectiveness, *Soil Dynamics and Earthquake Engineering* 18 (1999) 1–10.
[30] R. Hildebrand, Asymptotic analysis of hard wave barriers in soil, *Soil Dynamics and Earthquake Engineering* 23 (2003) 143–158.
[31] S. Anand, S.L. Kee, J.G. Wang, S.H. Chew, Z.W. He, H.W. Tan, Field trial assessment for performance of soft porous layers on ground shock reduction, PARARI 2007, Australia.
[32] T.W. May, B.A. Bolt, The effectiveness of trenches in reducing seismic motion, *Earthquake Engineering and Structural Dynamics* 10 (1982) 195–210.
[33] H. Takemiya, Field vibration mitigation by honeycomb WIB for pile foundations of a high-speed train viaduct, *Soil Dynamics and Earthquake Engineering* 24 (2004) 69–87.
[34] J. Lysmer, R.L. Kuhlmeyer, Finite dynamic model for infinite media, *Journal of Engineering Mechanics Division—ASCE* (1969) 859–877.
[35] E.D. Giroux, HEMP User's Manual, University of California, LLNL Report. UCRL-51079, 1973.
[36] A. Tadeu, P. Santos, J. Antonio, Amplication of elastic waves due to a point source in the presence of complex surface topography, *Computers & Structures* 79 (2001) 1697–1712.